

Specific Heat Capacity Determination by DSC

April 19, 10:00am - 11:00am EDT

Specific heat capacity (c_p) is an important, temperature-dependent material property and is often specified in material data sheets. It is a key property for improving technical processes such as injection molding, spray drying, or crystallization, as well as for the safety analysis of chemical processes and the design of chemical reactors.

Watch this session during the WAS Virtual Conference:



Dr. Jürgen Schawe

[Register Now](#)

This talk is sponsored by **METTLER TOLEDO**

An Artificial Neuromuscular System for Bimodal Human–Machine Interaction

Sunyingyue Geng, Shuangqing Fan,* Hangfei Li, Yashuai Qi, Chunhua An, Enxiu Wu, Jie Su,* and Jing Liu*

Neuromuscular system enabled muscle functions are critical for body movements, such as rhythmic motions and other complexed movements. Imparting artificial neuromuscular system to advanced robots and interactive systems can potentially improve their sensorimotor coordination and interactivity. Here, an artificial neuromuscular system is reported to mimic the sensing, processing, and manipulation of neuromuscular information, which consists of a triboelectric nano-generator (TENG), SnErO_x neuromorphic transistors (SENTs), and the signal-converting system. The synaptic performance of the SENT is optimized to implement multiple operation modes of muscle upon receiving signals from TENG, including muscle contraction, fast/slow muscle fiber shift, conscious/unconscious muscle movements, and transformation. As a proof-of-concept demonstration, the artificial neuromuscular system is used to develop contact human–machine interaction (HMI) by decoding the surface electromyogram (sEMG) and non-contact HMI based on supercapacitive iontronic effect. Importantly, both HMI demonstrate real-time gesture recognition and robotic manipulation, indicating the potential of developing next-generation smart electronics that desire multiple interaction patterns.

and process real muscle signals efficiently.^[5] In a biological neuromuscular system, external stimuli received by somatosensory are encoded as neural spikes and processed by neurons and synapses using a series of intelligent functions, such as adaptation, filtering, amplification, and storage. It is then transmitted to the nerve center for further processing, which realizes high-level functions, such as classification, identification, and learning (Figure 1). Such sophisticated neuromuscular control system allows muscles to perform complex tasks, such as contraction, precision grip, and complex gesture coding, upon perceiving bioelectric signals and tactile patterns through touching and interacting. Integration of neuromuscular system into the embodiment of HMI systems may transform them into intelligent machines which, for instance, can use sensory neurons to detect environmental cues to respond and orchestrate various motor

patterns adaptively through their neural circuitry.^[6–8]

Recently, advances in electronic devices have boosted the development of artificial neuromuscular systems, which enable HMI the capabilities of self-learning, self-powering, self-adapting, etc.^[4,7,8] For example, Lu et al. developed a HMI by anchoring multilayer graphene into electro-spun polyamide, which worked in noncontact mode for asthma detection, remote alarm and medicine delivery for bedridden patients with the help of a software algorithm.^[2] Niu et al. proposed a human-robot interaction system by using motivated full-skin bionic e-skin and deep learning to identify gesture and material species in real time.^[9] Zhang et al. presented a wearable and self-powered HMI based on a flexible-electromagnetic generator, which realized remote gesture recognition through machine learning.^[10] However, these reported systems have biological signal acquisition and signal processing parts separated, and the latter of which was usually based on classical von Neumann systems consuming a considerable amount of time and power.^[11–16] Future development of intelligent HMI systems requires near-sensor or in-sensor neural computing solutions to allow real-time sensory processing with low communication latency and low power consumption. In this sense, there is a great need to develop intelligent neuromuscular systems with intrinsic capabilities of neuromorphic perception and recognition, preferably implemented at the device level. Such a system would benefit the realization of muscle behavior mimicry and


1. Introduction

Human–machine interaction (HMI) is an emerging interface that aims to make the interactions between humans and robots/machines smart and simple.^[1–4] To achieve such goal, it is important to generate artificial muscle signals accurately,

S. Geng, S. Fan, H. Li, Y. Qi, J. Su
College of Physics and College of Electronics & Information
Qingdao University
Qingdao 266071, China
E-mail: sqfan@qdu.edu.cn; jsu@qdu.edu.cn

S. Geng, E. Wu, J. Liu
State Key Lab of Transducer Technology
Shanghai Institute of Microsystem and Information Technology
Chinese Academy of Sciences
Changning Road 865, Shanghai 200050, China
E-mail: jingliu_1112@tju.edu.cn

C. An, E. Wu, J. Liu
State Key Laboratory of Precision Measurement Technology and Instruments
School of Precision Instruments and Opto-Electronics Engineering
Tianjin University
No. 92 Weijin Road, Tianjin 300072, China

 The ORCID identification number(s) for the author(s) of this article can be found under <https://doi.org/10.1002/adfm.202302345>.

DOI: 10.1002/adfm.202302345

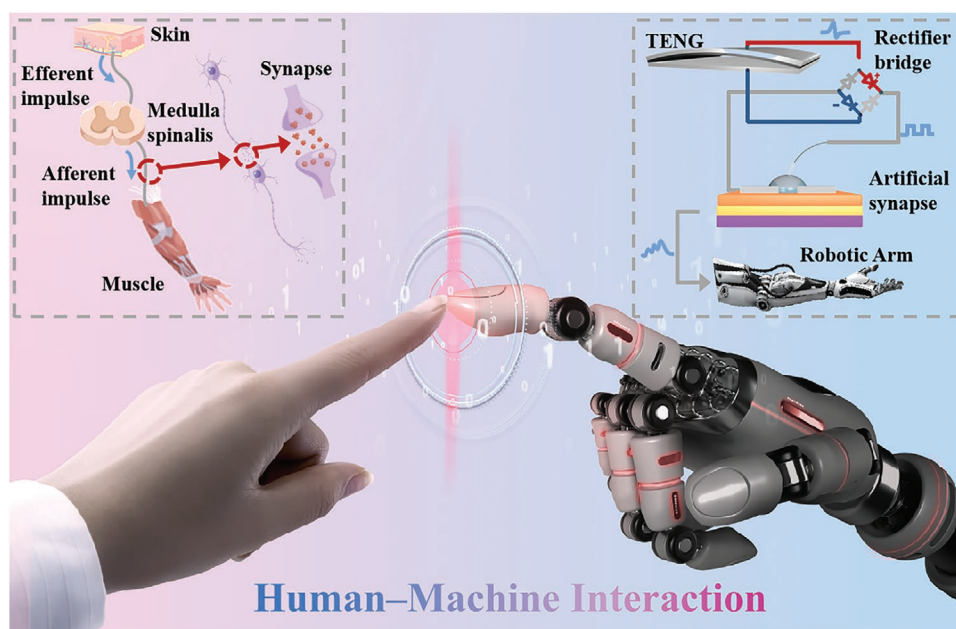


Figure 1. Artificial HMI system mimicking a neuromuscular control system.

human-like cognition to help achieve dexterous manipulation and gesture interaction.

Here, we describe an intelligent neuromuscular system based on triboelectric-nano-generator (TENG) and synaptic transistors (Figure 1). The flexible TENG is used to simulate the biological tactile sensing system, which collects data from multiple tactile receptors and transmits them to SnErO_x neuromorphic transistor (SENT, act as nerve center) for data processing and actuator control. First, the electrical properties of SENT were optimized by tuning the Er^{3+} concentration in the SnErO_x to achieve low-power signal transmission and processing. Then, multiple functions of muscle were mimicked by TENG-SENT neuromuscular system, including muscle contraction (single twitch, incomplete tetanic contraction, and complete tetanic contraction), fast/slow muscle fiber shift, conscious/unconscious muscle movements, as well as muscle hypersensitivity/allodynia and recovery. Furthermore, surface electromyography (sEMG) identification and gesture pattern recognition were both demonstrated by the TENG-SENT system. Benefiting from these capabilities, both contact mode HMI based on sEMG identification and noncontact mode HMI based on the supercapacitive iontronic effect were successfully developed. This work provides a new scheme for real-time and low power consumption muscle-based HMI system.

2. Results and Discussion

2.1. Performance Optimization of the SENT

Figure 2a shows the schematic cross-section of the SENT. It is fabricated by depositing SnErO_x thin film on a substrate and drop-casting $\text{PEO}:\text{LiClO}_4$ ion gel as the gate dielectric layer. An illustration of the atomic arrangement in the $\text{SnEr}_{2\%}\text{O}_x$ and SnO_2 channel is shown below the channel with enlarged view.

It explains the role of Er^{3+} played in the $\text{SnEr}_{2\%}\text{O}_x$ film, which suppresses the formation of oxygen vacancies (i.e., shallow electron donors), resulting in reduced electron doping in the film. In order to optimize the device performance, a series of SnO_2 TFTs with different Er^{3+} concentrations were fabricated on $\text{SiO}_2/p^+\text{-Si}$ wafers. The electrical characteristics as a function of Er^{3+} -doping content are summarized in Figure S1 (Supporting Information). It is noted that the pristine SnO_2 TFT exhibits large off-state current (I_{off}) of $\approx 10^{-6}$ A, resulting in the poor $I_{\text{on}}/I_{\text{off}}$ of $\approx 10^3$ (Figure S1a, Supporting Information). The large I_{off} leads to high static and dynamic power dissipation and is therefore unexpected. Er^{3+} doping with was found to effectively decrease the electron concentration of the TFT at the off state, resulting in the improved current modulation capability. However, as Er^{3+} doping concentration increased to 5 at.%, the V_{TH} shifted positively to near to 0 V, and thus, the device changed from depletion mode to enhancement mode. Since depletion mode is preferred for neuromorphic circuitry emulating to simplify circuitry design and lower power consumption, 2 at.% Er^{3+} -doped SnO_2 TFT (written as $\text{SnEr}_{2\%}\text{O}_x$) was chosen as the optimal device for the subsequent research.

To evaluate the superiority of $\text{SnEr}_{2\%}\text{O}_x$ in neuromorphic transistor (SENT), the comparison of synaptic transistor properties between $\text{SnEr}_{2\%}\text{O}_x$ and SnO_2 was presented and analyzed in Figure 2b–f. Figure 2b plots the drain current variation of neuromorphic transistor as a function of gate voltage with and without Er^{3+} doping, the key parameters of which are extracted and shown in Figure 2c. Compared to pristine SnO_2 device, $\text{SnEr}_{2\%}\text{O}_x$ exhibited superior electrical performance, including higher $I_{\text{on}}/I_{\text{off}}$ ratio ($\approx 5 \times 10^5$) and smaller subthreshold swing (250 mV dec^{-1}), which strongly relates to the interface trap density at the ion gel/channel interface. When the interface trap density is high, more electrons in the channel can be captured in the traps to increase SS value. Therefore, the interface trap density can be extracted from the SS value,

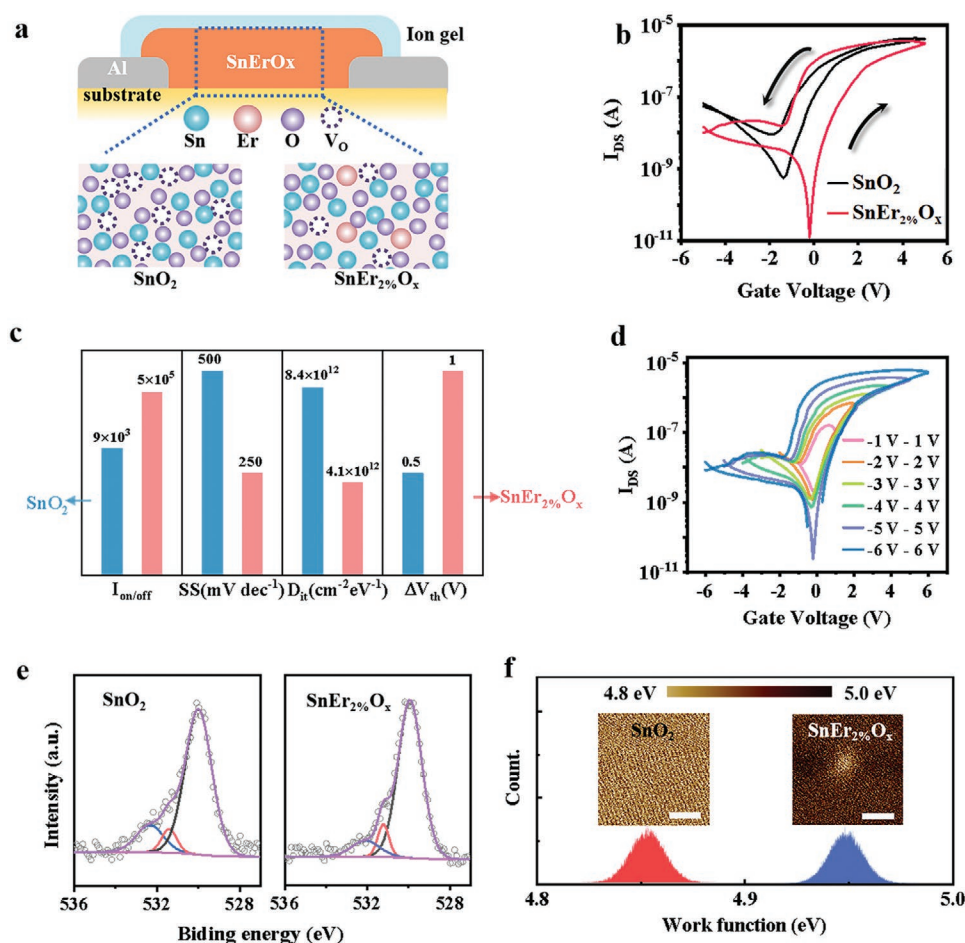


Figure 2. Electrical performance of doped SENT. a) Schematic cross-section of the SENT and atomic arrangement of SnO₂ and SnEr_{2%}O_x. b) The transfer curve of SnO₂ and SnEr_{2%}O_x TFT. c) Histograms of $I_{on/off}$, SS , D_{it} , and ΔV_{th} values of SnO₂ and SnEr_{2%}O_x TFT. d) Transfer curves of SENT with different gate voltage sweeping ranges. e) Oxygen 1s XPS peaks with best-fit results. f) KPFM images, histograms, and work function of SnO₂ and SnEr_{2%}O_x thin film. Scale bar: 1 μ m.

which shows significant reduction ($\approx 50\%$) of mean value from $8.35 \times 10^{12} \text{ cm}^{-2} \text{ eV}^{-1}$ (pristine SnO₂) to $4.12 \times 10^{12} \text{ cm}^{-2} \text{ eV}^{-1}$ (SnEr_{2%}O_x). The detailed calculation process can be found in the Experimental Section. Furthermore, the hysteresis was measured from the transfer curves. Within ± 6 V gate bias, SnO₂ showed small variations in V_{th} of 0.5 V, which remarkably enlarged to 1 V after the Er³⁺ doping, corresponding to an expansion of $\approx 200\%$. Figure 2d shows the dual-swept transfer curves of the SnEr_{2%}O_x under various gate bias sweeping range, in which the ΔV_{th} increased with the enlargement of the gate voltage sweeping range, due to the increased number of Li⁺ and ClO₄⁻ ions activated within the electrolyte. Therefore, enhanced electrical and synaptic characteristics are expected.

In order to investigate how Er cation affects SnO₂ film composition and oxygen bonding, four types of SnO₂ films with different Er³⁺ concentrations were prepared and performed X-ray spectroscopy (XPS) analysis as shown in Figure 2e. In Figure 2e, the O 1s peaks can be consistently deconvoluted into three individual subpeaks reflecting different O environments. The dominant peak centered at 530.0 eV arises from O atoms bonded to the nearest-neighboring metal ions (M–O–M) in the lattice, the peak at 531.4 eV is attributed to O atoms in the

vicinity of an O vacancy, and the peak at the highest binding energy of 532.3 eV can be assigned to surface O, such as hydroxyls (M–OH). To achieve superior electrical performance, metal oxide semiconductors usually maximize M–O–M formation/densification and minimize the detrimental O vacancies and M–OH densities. Thus, an instructive method to correlate XPS results with SENT performance is to compare the area ratio of the O 1s subpeak with the lowest binding energy (corresponding to M–O–M) to the entire O 1s peak, which is defined here as η_{M-O-M} . As shown in Figure S2 (Supporting Information), after Er³⁺ doping, the η_{M-O-M} increased from 75.3% to 83.1%. This trend is consistent with the aforementioned electrical performances of SENT, which indicates that Er³⁺ acts as an effective O vacancy (trap states) suppressor due to the strong Er–O bonding. Kelvin probe-force-microscopy (KPFM) was used to investigate the effect of Er³⁺ concentration on the band structure of SENT as shown in Figure 2f. The contact potential difference (V_{CPD}) between the KPFM tip and the samples was measured, which can be converted to the work function (Φ) using the relation $\Phi_{\text{sample}} = \Phi_{\text{tip}} - eV_{CPD}$. After 2 at.% Er³⁺ doping, the Φ increases from 4.86 to 4.95 eV, which in turn shifts V_{th} to a positive voltage. This shift can

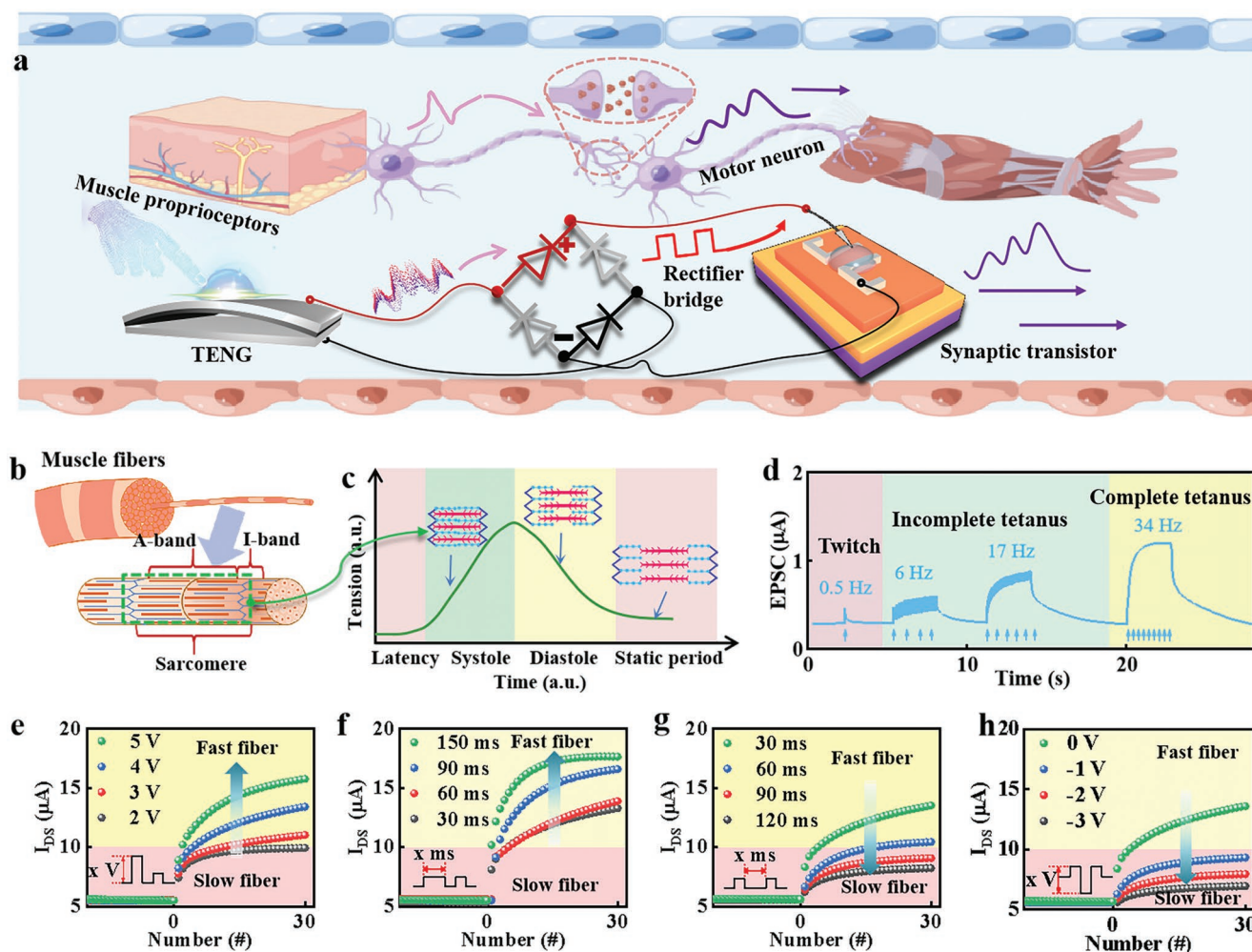


Figure 3. Muscle function simulation based on the artificial neuromuscular control system. a) Schematic illustration of the neuromuscular control system (upper panel) and the corresponding artificial neuromuscular system (lower panel). b) Schematic diagram of muscle fibers. c) Muscle fiber length in accordance with resting time in a single twitch. d) EPSC (i.e., motor unit force) produced by artificial neuromuscular system. The sigmoidal relation between stimulation frequency (0.5–34 Hz) of TENG and the EPSC (correspond to motor unit force) of SENT. Simulation of e) slow to fast myofiber shift with increased stimulus amplitude and f) duration time of pulses. g, h) Simulation of fast to slow myofiber shift with increased interval time (g) and opposite pulses.

be explained by the band structures as shown in Figure S3 (Supporting Information). Since the SnO_2 channel has a narrow gap between the conduction band edge (E_c) and the Fermi level (E_F), it is possible to bend the E_c below E_F by applying a positive gate bias. On the contrary, the SnO_2 channel with Er^{3+} doping results in a large gap between the E_c and E_F , which prevents the E_c from being bent below E_F , which explains the decrease in I_{off} current of SENT with Er^{3+} doping.

2.2. Muscle Function Simulation

Mimicking the operation mechanism of muscle has been of great interest for applications in robotics and HMI systems.^[17] For biological muscle, the proprioceptors located in muscle convert stimulation into the action potential of motor neurons. As a result, information is transmitted from the nervous system to the muscle system, causing changes in muscle fibers, and

thus, limb response. To realize the above biological function, an artificial neural circuit consisted of a TENG receptor and a SENT motor neuron was constructed as shown in Figure 3a. The TENG generates electrical potential upon pressure, which simulates the muscle proprioceptors. Its working principle and open-circuit voltage as a function of applied pressure (80–300 Pa) is presented in Figures S4 and S5 (Supporting Information), respectively, indicating its stable and high output voltage. The action potential (presynaptic pulses) produced by the TENG is transmitted to the artificial synapse (SENT) through bridge circuit, which then generates excitatory postsynaptic potential. The working mechanism of the TENG-SENT system is illustrated in Figure S6 (Supporting Information). The excitatory postsynaptic current (EPSC) of the system under various types of stimuli were tested and presented in Figure S7 (Supporting Information), suggesting its stability.

Furthermore, the system is used to simulate advanced functions of muscle. Physiologically, muscle is composed of bundles

of myofibers, which are then built by concentrically aligned sarcomeres as shown in Figure 3b. The sarcomere can be divided into light (I) and dark (A) bands, which aligned alternatively to enable muscle contractility.^[18] Specifically, when a suprathreshold stimulation is given to the muscle proprioceptor, the I-band becomes either longer or shorter, corresponding to the traction or contraction response of muscle, while the A-band remains unchanged. Figure 3c shows the change of tension during a muscle contraction process, which is divided into four periods of latency, systole, diastole, and static in biology. The corresponding myofibrils schematic is also shown in each period. Since the time required to complete a contraction process is much longer than to apply an action potential, the contraction triggered by the sequential action potential can be superimposed on the previous contraction as the frequency of the action potential increases. As shown in Figure 3d, three different forms of contraction were simulated under electrical stimulations with different frequencies. With a low stimulation frequency of 0.5 Hz, the SENT is always stimulated at the static period, resulting in a monodispersed EPSC peak, which is called single twitch in the contraction reaction of the muscle. By applying moderate frequency (6–17 Hz), the sequential stimulation is superimposed on the diastolic period of the previous response, which is similar to incomplete tetanic contractions. In contrast, as the stimuli repetition frequency is above 34 Hz, the sequential stimulation is superimposed on the systole period, and EPSC linearly increases to saturation, leading to a single broad peak (i.e., complete and uniform tetanic contractions). The success of the SENT in simulating biological muscle contraction is because that the maximal and sustained EPSC can be generated by Li^+ accumulation during tetanic high-frequency stimulation,^[19] similar to the Ca^{2+} mediated modulation of muscle contraction.^[20]

Besides muscle contractile activity, different stimuli can also induce transition of muscle types. According to the general adaptation syndrome (GAS) theory, muscle can transit between fast and slow fiber types with physical exercise-based training.^[21] Specifically, anaerobic exercise is believed to induce a slow-to-fast transition in fiber composition, while aerobic exercise can cause a transition from fast-to-slow fiber type. In order to simulate this biological fast/slow fiber-type transition, our artificial nerve system is trained by a series of voltage pulses with different pulse amplitude, duration time (T_d), and interval time (ΔT). All raw data is recorded and plotted in Figure S8 (Supporting Information), while the corresponding output current under a constant read voltage of 2 V is extracted and shown in Figure 3e–h. As shown in Figure 3e, a series of electrical pulses ($V_{GS} = 2, 3, 4$, and 5 V, $T_d = 30$ ms) corresponding to aerobic exercise is applied to the gate electrode of the SENT, after which the sensitized current response curves are measured at $V_{GS} = 2$ V. The SENT exhibits enhanced output current with increased stimulating pulse voltage from 2 to 5 V, which mimics the process of slow-to-fast fiber type transition induced by intense energetic exercise. The increase of pulse duration corresponding to extending the exercise time ($T_d = 30, 60, 90$, and 150 ms, $V_{GS} = 4$ V) can further promote the transition from slow to fast fiber type as shown in Figure 3f. In contrast, fast fibers can switch back to slow fibers when rest periods are increased or aerobic exercise is performed. Figure 3g

demonstrates that the EPSC amplitude decreases gradually as the duration between training pulses increases (ΔT increases from 30 to 120 ms). The fast-to-slow fiber transition could be further accelerated by applying opposite pulses (V_{GS} range from 0 to -3 V) representing aerobic exercise as shown in Figure 3h.

2.3. Unconscious and Conscious Muscle Movement Simulation

Neurobiologically, the control of muscle can be divided into unconscious (passive) and conscious (active) forms. One important unconscious muscle action is rhythmic motor with unconsciously performed repetitive action. Many rhythmic motor behaviors require spatiotemporally coordinated contraction of multiple groups of muscles throughout the central pattern generators (CPGs), which is crucial for the HMI systems.^[22] As shown in Figure 4a, we simulated the rhythmic motor of the cat walking using our artificial CPG, in which TENG works as an adaptive frequency oscillator to generate rhythmic signals, while four SENTs act as nerves in the muscles of extremities to control muscle activities. Rhythmic stimulations are applied to stimulate TENG ($V_{TENG} = 3$ V, $T_d = 0.5$ s, 4 pulses per step, representing simulation the of limb motoneurons) according to the coordinated motor program of cat. Then, four basic gaits of cat with different speed are mimicked, which are walking, trotting, pacing, and galloping. The step cycle for an individual leg includes two phases of swing and stance. The swing phase (electrical active phase as shown in lower panel of Figure 4a) corresponds to the phase when the foot is off ground and moving forward, while the stance phase (electrical silence phase in lower panel of Figure 4a) is the phase when the foot is on the ground and moving backward with respect to the body.^[23] During walking, trotting, and pacing, the two hind legs move alternatively with respect to each other as the two forelegs do (see the upper panel of Figure 4a). Therefore, the speed of progression is primarily determined by the time spent in the swing and stance phases. These muscle movements are genetically predetermined and occur “spontaneously”, independent of experience.

On the other hand, sending the Morse code is one type of consciously controlled muscle movement, which is simulated by the TENG-SENT system through encoding “MUSCLE” as shown in Figure 4b. The Morse code uses dots, dashes, and different durations between sequences to encode text characters through consciously controlling finger tapping. The international Morse code of 26 letters is shown in Table S1 (Supporting Information). In our TENG-SENT system, voltage stimuli with different amplitude can be generated by manipulating the strength of pressure exerted on TENG (as shown in Figure S9, Supporting Information), which then activate different EPSC peak modes with different amplitudes in the SENT. The peak with low amplitude corresponds to a dot, while the peak with high amplitude corresponds to a dash. Consequently, the combinations of these two peaks can encode all the letters (as shown in Figure S10, Supporting Information).

Moreover, repetitive training can transform conscious muscle movement into unconscious muscle memory. To mimic this conversion process, a 9×9 SENT array is constructed as shown in Figure 4c. When the letter “M” is inputted into the array,

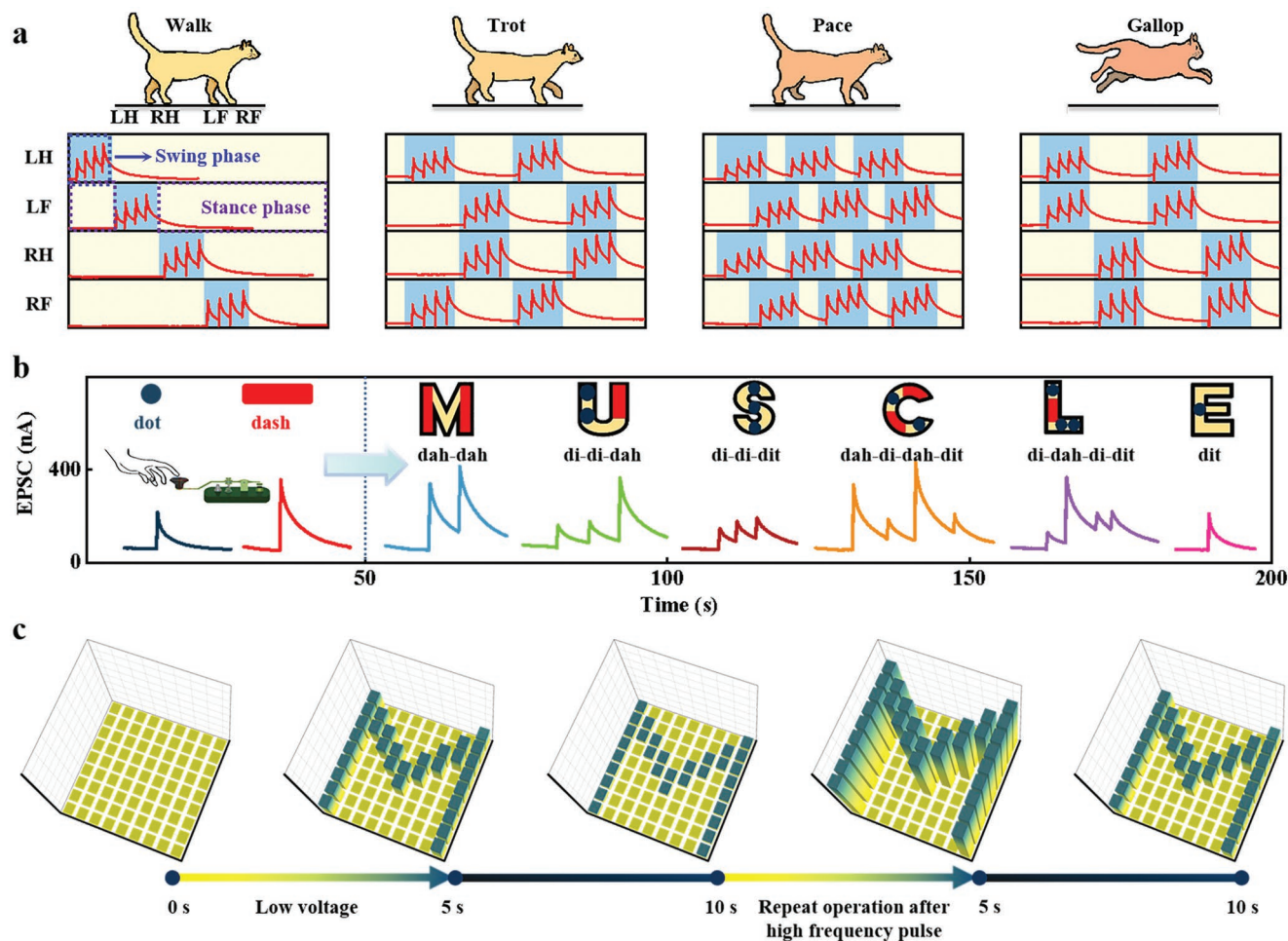


Figure 4. Simulation of unconscious and conscious muscle movement. a) The simulation of unconscious stepping patterns of the cat: walk, trot, pace, and gallop. b) The simulation of consciously code "MUSCLE" in international Morse code. c) The simulation of muscle memory forming process using 9×9 artificial synaptic arrays.

the 81 pixel image formed by the array is refreshed in a short time due to the exemplary short-term plasticity of the SENT. As the frequency of tapping pulse increases, the synaptic weights increase rapidly, leading to success information retrieve after 5 s with slight loss, which demonstrates the transformation of conscious muscle movement to unconscious muscle memory.

In addition to memory behavior, the muscle also showed sensitization and recovery properties to pains. The muscle sensitization refers to the reduced threshold (allodynia) and augmented response (hyperalgesia) to external stimuli after noxious stimulus (injuries), which is related to the increased Ca^{2+} in sarcoplasmic reticulum.^[24–28] As shown in Figure S11a (Supporting Information), EPSC amplitude was first measured at different voltages (1–6 V) to represent the normal state. Subsequently, a series of pulses (2 V or 4 V, $T_d = 30$ ms, 20 pulses) was applied to the same synaptic device, representing the noxious training. After that, the EPSC was measured again under the same voltages of 1–6 V which showed different level of sensitivity to pains. Figure S11b–d (Supporting Information) extracts the maximum EPSC value of each pulse in Figure S11a (Supporting Information) under normal state and after

different levels of noxious injuries. Figure S11b (Supporting Information) shows that the threshold voltage reduced as the noxious injuries became stronger (amplitude increased from 2 to 4 V), which emulates the decreased endurance to pain after injury (allodynia). Meanwhile, as compared to the normal state (red area), the amplitude of the EPSC was significantly increased after noxious injuries (yellow area and blue area). Moreover, the stronger the injury, the higher the EPSC (hyperalgesia). The decreased endurance and enhanced response to pain mimic the sensitization feature of muscle. Meanwhile, the duration (Figure S11c, Supporting Information) and numbers (Figure S11d, Supporting Information) of injuries also play important roles in the sensitization behavior of our synaptic transistor as shown in Figure S11c,d (Supporting Information), respectively.

The post-traumatic recovery function of muscle is demonstrated in Figure S11e–h (Supporting Information). A series of injury pulses (2 V, $T_d = 30$ ms, 20 pulses) is applied to the synaptic transistor, introducing a change that emulates the pre-injury to the muscle (Figure S11e, Supporting Information). The EPSC of the same device were recorded under the

voltage of 1–6 V after different recovery time ($\Delta T = 120, 210$, and 300 ms). The EPSC responses are shown in Figure S11f (Supporting Information). As the recovery time increased, the threshold voltage and the EPSC value became higher and lower, respectively, which undergoes an opposite process to the allodynia and hyperalgesia behavior (i.e., recovery). When the recovery time equals to 300 ms, the EPSC becomes close to the normal state (red area in Figure S11f, Supporting Information), indicating the muscle relaxed back to its undamaged state. In addition, muscle recovery can be accelerated by applying an opposite voltage (muscle therapy). Figure S11g,h (Supporting Information) shows that increased opposite voltage amplitude (Figure S11g, Supporting Information) and pulses number (Figure S11h, Supporting Information) can both promote the muscle recovery. These results indicate that our synaptic transistor successfully simulated the process of muscle recovery from injuries.

2.4. Construction of Wired HMI Based on sEMG Recognition

As a proof-of-principle demonstration, we constructed a bioelectric controlled HMI system, including three-electrodes filled with electrolyte paste, a pre-treatment circuit, SENT arrays, and a robotic hand. Figure 5a,b and Figure S12 (Supporting Information) show the circuit diagram and photograph. The bandwidth of the recording system is 1–1000 Hz with a sampling rate of 500 Hz for sEMG collection. Three sets of hand gestures are performed by the left hand of a tester, including from the open hand to the clenched fist, from half clenched to clenched fist, and sustained clenching fist. Each gesture is maintained for 50 s, which is followed by a 100 s rest interval to avoid fatigue. Figure 5c,d presents the sEMG signals for the three types of muscle movement during the flexion and extension of the hand, which is obtained through the gel electrodes attached on the wrist (Movies S1, Supporting

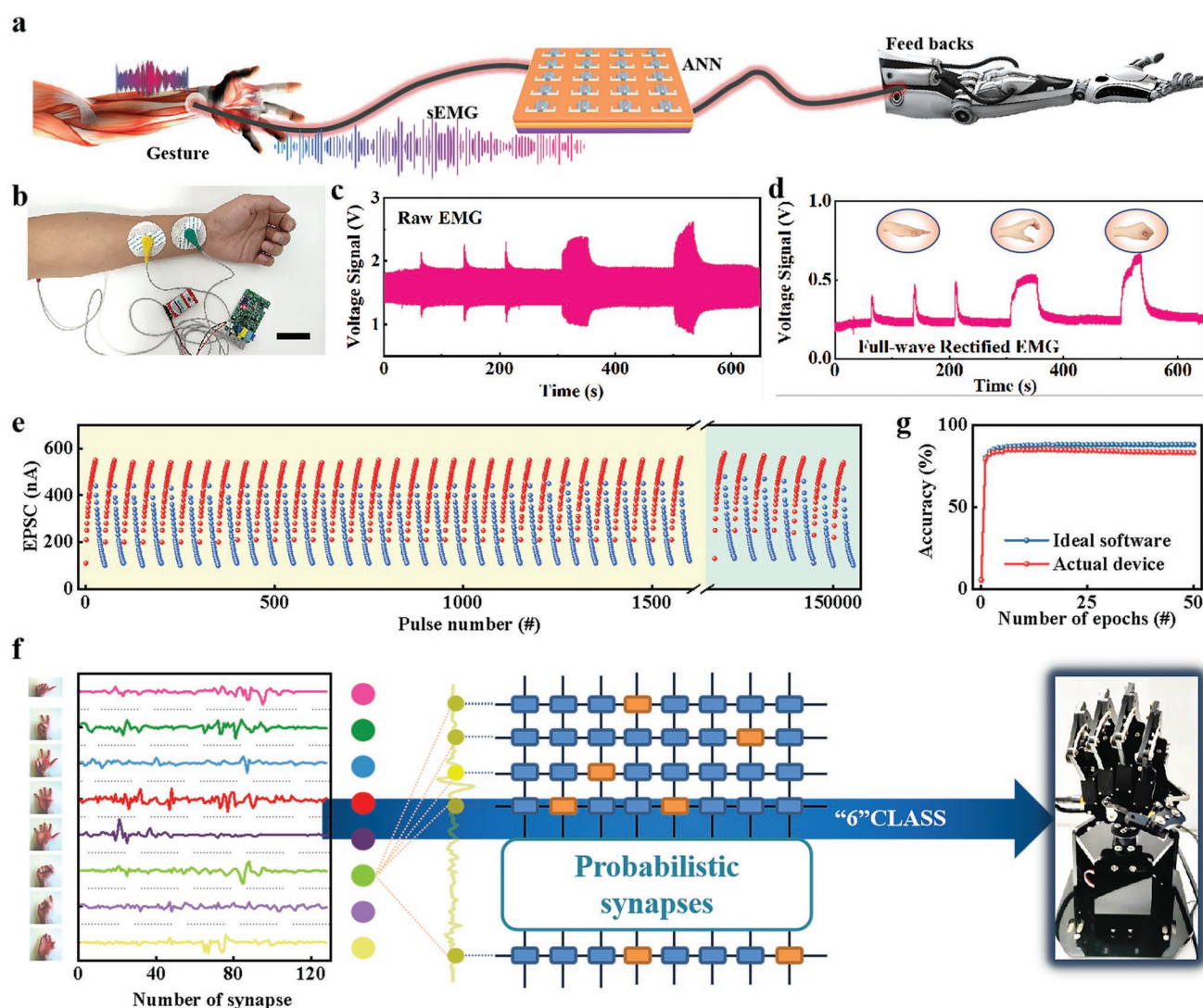


Figure 5. Construction of contact HMI by decoding surface EMG signal. a) Schematic diagram of contact HMI. b) Photograph of sEMG signal acquisition device. Scale bar: 5 cm. c) Raw data of sEMG signal during different grasping movement. d) Full-wave rectified sEMG signals. (Inset: three types of grasping movement.) e) Consecutive transitions of LTP/LTD during >3000 cycles. f) Demonstration of the contact HMI for sEMG recognition and robot controlling via neuron network structure. g) Recognition accuracy for the sEMG patterns during 50 epochs.

Information). Before the spectral analyses, sEMG data is band-pass filtered from 30 to 300 Hz (Figure 5c). Afterward, sEMG was full-wave rectified (Figure 5d). These signals exhibit a shape similar to the three forms of muscle contraction shown in Figure 3d, including single twitch, incomplete tetanic contraction and complete tetanic contraction. The processed information is used as the input of neural morphological classification array. The outputted signal is finally transmitted to the manipulator to realize HMI.

A central assumption in neurobiology holds that the changes in the weight of individual synapses underlie changes in behavior. This concept is widely accepted in the case of learning and memory where LTP and LTD are the most compelling mechanisms. Figure 5e shows the repeated conversion between LTP and LTD when consecutive presynaptic peaks are applied alternately (corresponding to 3000 cycles), one of which is composed of 25 enhancement peaks ($V_{GS} = 1$ V) and 25 inhibition peaks ($V_{GS} = -1$ V). Although there is a small decrease in the last few cycles, the difference from the initial state is almost negligible. This capability can be used to conduct pattern recognition of sEMG signals from muscle. The second database (DB2) from the NinaPro (Non-Invasive Adaptive Prosthetics) project is selected here and normalized for recognition,^[29] which includes sEMG data related to eight isometric and isotonic hand configurations (Figure 5f). In order to decode sEMG signals more effectively and accurately, SENT array-based neural network is used to analyze the shape characteristics of each signal. The network is composed of 128 inputs (corresponding to the number of synaptic weights) and 8 output neurons (corresponding to 8 sEMG categories), which are connected by SENTs. Figure 5g shows an example of identifying the sEMG of fingers flexed together in fist (class 6), which is then further translated to manipulate a commercial robotic hand model (called uHand) for recapitulating dynamics of the corresponding hand gestures. After 50 epochs, the fist-clenching movement can be accurately recognized when sEMG is recorded with high accuracy (mean accuracy = 87.8%), which is close to the recognition accuracy using the ideal synaptic device. The corresponding confusion matrix is shown in Figure S13 (Supporting Information), showing the successful classification of eight sEMG categories. After receiving the command from the neural network, uHand responded accordingly to the real-time signals (Movie S1, Supporting Information).

2.5. Construction of Non-Contact HMI Based on Remote Gesture Recognition

Wired HMI is generally restricted by the interaction distance and contact quality between electrode and skin due to mechanical wear and fatigue. Thus, a non-contact HMI based on single electrode TENG (SETENG)-SENT neural network was developed for real-time gesture recognition, which can provide a natural and unconstrained interaction for complexed and enriched information recognition in 3D space (Figure 6a,b).^[10,30] The mechanism of SETENG is very similar to that of double-electrode TENG mentioned above (see Figure S14, Supporting Information). In this model, SETENG converts movement information of hand into direct current (DC) voltage through

bridge circuit, while SENT performs signal conversion and neuromorphic manipulation to simulate body motor perception. The detected signals are then used to control the motion of the uHand. First, the impact of electrostatic induction on the output signal of SETENG was investigated. The human skin works as a tribo-positive material, while the polyethylene terephthalate (PET) acts as a tribo-negative material. Before the operation, the PET was negatively charged by tapping it with a human finger. Subsequently, when the human palm approaches the negative triboelectric layer, the potential difference between the electrode layer and the ground causes the flow of electrons, resulting in an electrical signal. As shown in Figure S15 (Supporting Information), the output voltage of the SETENG enhances as the area of the palm increased from 10 to 150 cm², which may be attributed to the increase of the electric field. On this basis, it is possible to realize in-air gesture recognition. When the tester made gestures in the order of scissors-rock-paper as shown in Figure 6c, the amplitude of the EPSC in the SENT gradually increased (see Figure 6d) because of the increased palm area. The decay of EPSC also slows down, representing a transition from short-term potentiation to long-term potentiation. The gesture-specific response of TENG-SENT makes it possible for local processing applications, such as smart autonomous robotics, in-sensor classification and prosthetic motion control, as well as for further processing and classification of hardware-based neural networks.

As shown in Figure 6e, to enhance the flexibility and efficiency of HMI, a convolution neural network (CNN) was constructed to analyze the shape feature of gestures that was extracted from sign language MNIST dataset (Figure 6f). The CNN architecture can roughly be split into three classes of input, convolutional backbone, and classifier head. In the convolutions with non-linear activation and max pooling layers, the grayscale information of input gestures is normalized to the range from -1 to +1 and then converted into positive/negative weight sequences as the network inputs. Here, the crossbar based on SENT arrays worked as a classifier head to perform the gesture classification task. Figure 6g shows that training a SENT-based CNN approaches ideal numerical accuracy (>80% training accuracy after 100 epochs), which is the theoretical limit for this algorithm. The corresponding confusion matrix is presented in Figure S16 (Supporting Information), demonstrating the successful classification of the 24 gesture classes based on the SENT hardware array. Intercept part of the confusion matrix (A–H) is shown in Figure 6h. The classified gesture signals from TENG and CNN allow wireless, real-time control of the uHand in Figure 6g (Movie S2, Supporting Information). Overall, the SETENG-SENT system shows great potential for various non-contact HMI applications, including control of a humanoid robot, drone, prosthetic hand, display interface, electronic wheelchair, and more.

3. Conclusion

To sum up, we designed an artificial neuromuscular system is constructed by integrating flexible muscle proprioceptors and synaptic device. The electrical properties of SENT were first optimized by tuning the Er³⁺ concentration in the SnErO_x

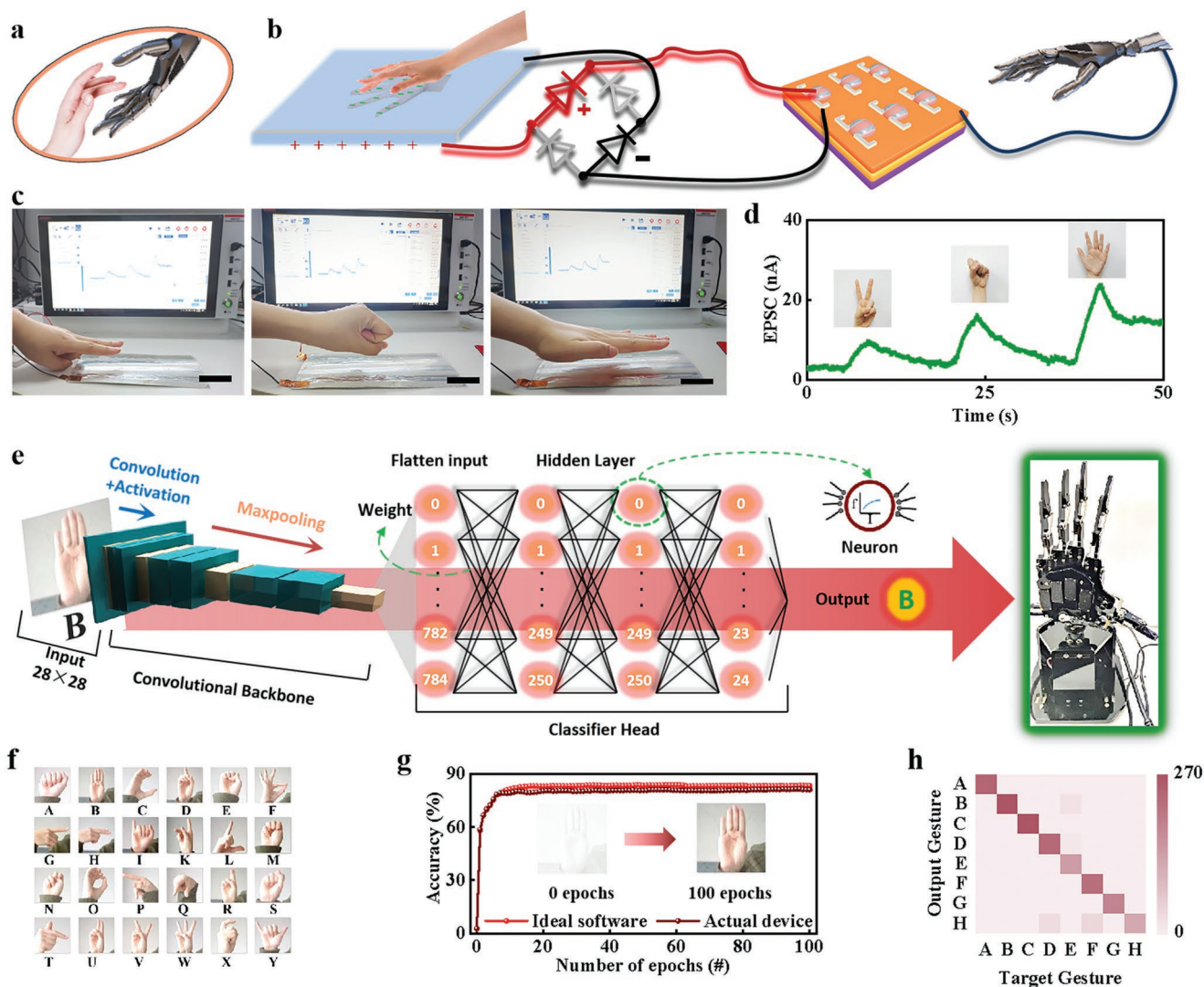


Figure 6. Demonstrations of gesture recognition and non-contact HMI. a,b) Schematic diagram of non-contact HMI. c) The test process of three non-contact gestures (scissors, rock, paper, scale bar: 5 cm). d) Induced EPSC of different gestures. e) CNN architecture for pattern recognition to facilitate robot control. f) Photographs of the gesture morphologies representing different English alphabets. g) Recognition accuracy for the gestures during 100 learning cycles of synaptic devices. (Inset: The feature mapping to recognize a gesture (representing “B”) before and after training). h) Confusion matrices for a classification test of the eight gestures (representing “A–H”) during 100 learning epochs.

to achieve low-power signal transmission and processing. With this artificial neuromuscular system, multiple operation modes of muscle, including muscle contraction (single contraction, incomplete tetanic contraction and complete tetanic contraction), fast/slow muscle fiber shift, conscious/unconscious muscle movements and transformation, as well as hypersensitivity/allodynia and recovery, were successfully emulated. In addition, the artificial neural network based on SENTs can be used to identify surface electromyography (sEMG) during muscle contraction and recognize hand gestures in noncontact model. Benefiting from these capacities of TENG-SENT neuromuscular system, both HMIs in contact mode based on sEMG signals and noncontact mode based on the supercapacitive iontronic effect are successfully developed.

4. Experimental Section

Preparation of Solution: First, erbium chloride hexahydrate ($\text{ErCl}_3 \cdot 6\text{H}_2\text{O}$) and tin chloride dihydrate ($\text{SnCl}_2 \cdot 2\text{H}_2\text{O}$) powder were completely dissolved in *N,N*-dimethylformamide (DMF) at room temperature in proportion to obtain the precursor solution. Then stir the mixed solution for 2 h under environmental conditions to obtain a uniform and transparent solution.

Device Fabrication: A heavily *p*-doped Si wafer with a thermally grown SiO_2 layer (300 nm) was used as the substrate. Before the device preparation, the substrate was cleaned with acetone through ultrasonic cleaning, then washed with ethanol and deionized water, and finally dried with N_2 . In order to obtain higher hydrophilicity, an O_2 plasma treatment was performed before spin-coating. The prepared precursor solution was filtered through 0.22 μm nylon-66 and coated on the substrate at 8000 rpm for 15 s. Then, ErSnO TFTs with different material atomic ratios were prepared by thermal annealing (200°C for 100 s and

600°C for 300 s). Then, with the assist of a shadow mask with a channel width of 1 mm and length of 100 µm, 60 nm Al electrodes were thermally evaporated.

Characterization and Measurements: XPS was conducted using an ESCALAB 250Xi instrument (Thermo Scientific). Keithley 4200 semiconductor characterization system conducted all electrical measurements. The output properties of TENG were measured by Keithley 4200 system electrometer. During the test, the device and the TENG should be well screened to avoid the electric surge from breaking down the transistor by the surrounding electrostatic charges. A ruler was used to control the approximate distance between TENG and palm in the experiment. SS were calculated using the formula: $SS = \frac{dV_{GS}}{d(\log I_{DS})}$, where I_{DS} is the S/D current, V_{GS} is the gate voltage. The trap density

(D_{it}) was extracted from the equation: $ss = \frac{kT \ln(10)}{q} \left(1 + \frac{q^2 D_{it}}{C_g} \right)$, where k

is the Boltzmann constant, T is the temperature, q is the electron charge, D_{it} is the density of interface trap, and C_g is the electrolyte capacitance. In order to collect sEMG data, the electrode system of the University of New Brunswick was worn on right arm, which consisted of four surfaces and a sEMG channel with a 1 kHz sampling frequency.

Device Simulations: The simulated artificial neural network was a four-layer network, and the back propagation algorithm was used for training. The input layer with 784 neurons, representing the 28×28 pixels of one hand gesture sample, was fully connected to a hidden layer with 250 neurons, which was then fully connected to an output layer of 24 neurons, representing 24 classes. Informed written consent was acquired for the wearable studies involving human participants and these conform to recognized standards of the Ethical Review Methods for Biomedical Research involving Humans adopted by the National Health and Family Planning Commission of the People's Republic of China.

Supporting Information

Supporting Information is available from the Wiley Online Library or from the author.

Acknowledgements

S.Y.Y.G. and S.Q.F. contributed equally to this work. This work was supported by the National Science Foundation of China (grant nos. 52075385, 62204134, and 62204170), National Key R&D Program (no. 2018YFA0307200), and the 111 Project (no. B07014). The authors would also like to thank S.Q.F. for drawing the parts of the human body. No ethical approval was needed for the experiments in this work, and the volunteer took part with informed consent.

Conflict of Interest

The authors declare no conflict of interest.

Data Availability Statement

The data that support the findings of this study are available from the corresponding author upon reasonable request.

Keywords

artificial neuromuscular, human–machine interactions, multiple operation modes, synaptic devices

Received: February 28, 2023

Revised: March 21, 2023

Published online:

- [1] B. T. Reid, J. Gibert, *Science* **2022**, 375, 149.
- [2] L. Lu, C. Jiang, G. Hu, J. Liu, B. Yang, *Adv. Mater.* **2021**, 33, 2100218.
- [3] S. An, H. Zhu, C. Guo, B. Fu, C. Song, P. Tao, W. Shang, T. Deng, *Nat. Commun.* **2022**, 13, 1446.
- [4] Y. Yu, J. Nassar, C. Xu, J. Min, Y. Yang, A. Dai, R. Doshi, A. Huang, Y. Song, R. Gehlhar, A. D. Ames, W. Gao, *Sci. Rob.* **2020**, 5, aaz7946.
- [5] S. Chun, J. S. Kim, Y. Yoo, Y. Choi, S. J. Jung, D. Jang, G. Lee, K. Il Song, K. S. Nam, I. Youn, D. Son, C. Pang, Y. Jeong, H. Jung, Y. J. Kim, B. D. Choi, J. Kim, S. P. Kim, W. Park, S. Park, *Nat. Electron.* **2021**, 4, 429.
- [6] T. Bruegmann, T. Van Bremen, C. C. Vogt, T. Send, B. K. Fleischmann, P. Sasse, *Nat. Commun.* **2015**, 6, 7153.
- [7] S. M. Mirvakili, D. Sim, I. W. Hunter, R. Langer, *Sci. Rob.* **2020**, 5, aaz4239.
- [8] Y. Chen, H. Zhao, J. Mao, P. Chirarattananon, E. F. Helbling, N. Seung, P. Hyun, D. R. Clarke, R. J. Wood, *Nature* **2019**, 575, 324.
- [9] H. Niu, H. Li, S. Gao, Y. Li, X. Wei, Y. Chen, W. Yue, W. Zhou, G. Shen, *Adv. Mater.* **2022**, 34, 2202622.
- [10] T. Zhang, Y. Ding, C. Hu, M. Zhang, W. Zhu, C. R. Bowen, Y. Han, Y. Yang, *Adv. Mater.* **2022**, 35, 2203786.
- [11] F. W. Hao, F. Cong, Y. Chang, R. Zhou, W. Zhang, G. Sun, P. Xu, Y. Qin, S. Ramakrishna, X. Liu, *Sci. China Mater.* **2023**, <https://doi.org/10.1007/s40843-022-2445-y>.
- [12] S. Fan, T. Xu, E. Wu, M. Cao, T. Liu, J. Su, *J. Mater. Chem. C* **2021**, 9, 16655.
- [13] S. Xin, Y. Chang, R. Zhou, H. Cong, L. Zheng, Y. Wang, Y. Qin, P. Xu, X. Liu, F. Wang, *J. Mater. Chem. C* **2022**, 11, 722.
- [14] R. Zhou, W. Zhang, H. Cong, Y. Chang, F. Wang, X. Liu, *Mater. Sci. Semicond. Process.* **2023**, 158, 107344.
- [15] L. Jiang, D. Dong, Y.-C. Lu, *Nano Res. Energy* **2022**, 1, 9120003.
- [16] S. Fan, J. Li, H.-Q. Cao, X. Liu, M. Cao, T. Liu, T. Xu, J. Su, *J. Mater. Chem. C* **2022**, 10, 14053.
- [17] Y. Kim, A. Chortos, W. Xu, Y. Liu, J. Y. Oh, D. Son, J. Kang, A. M. Foudah, C. Zhu, Y. Lee, S. Niu, J. Liu, R. Pfaffner, Z. Bao, T. W. Lee, *Science* **2018**, 360, 998.
- [18] A. F. Huxley, R. Niedergerke, *Nature* **1954**, 173, 971.
- [19] J. Safaei, G. Wang, *Nano Res. Energy* **2022**, 1, 9120008.
- [20] S. Ebashi, M. Endo, *Prog. Biophys. Mol. Biol.* **1968**, 18, 123.
- [21] H. Selye, *Nature* **1950**, 1, 1383.
- [22] F. Ruppert, A. Badri-Spröwitz, *Nat. Mach. Intell.* **2022**, 4, 652.
- [23] K. Pearson, *Sci. Am.* **1976**, 235, 72.
- [24] T. Graven-Nielsen, L. Arendt-Nielsen, *Nat. Rev. Rheumatol.* **2010**, 6, 599.
- [25] J. H. Yoon, Z. Wang, K. M. Kim, H. Wu, V. Ravichandran, Q. Xia, C. S. Hwang, J. J. Yang, *Nat. Commun.* **2018**, 9, 417.
- [26] X. Xu, E. J. Cho, L. Bekker, A. A. Talin, E. Lee, A. J. Pascall, M. A. Worsley, J. Zhou, C. C. Cook, J. D. Kuntz, S. Cho, C. A. Orme, *Adv. Sci.* **2022**, 9, 2200629.
- [27] K. Wang, W. Xu, W. Zhang, X. Wang, X. Yang, J. Li, H. Zhang, J. Li, Z. Wang, *Nano Res. Energy* **2022**, 2, 9120042.
- [28] X. Cai, S. Wang, L.-M. Peng, *Nano Res. Energy* **2023**, 4, 88.
- [29] M. Atzori, A. Gijsberts, C. Castellini, B. Caputo, A. G. M. Hager, S. Elsig, G. Giatsidis, F. Bassetto, H. Müller, *Sci. Data* **2014**, 1, 140053.
- [30] X. Guo, X. Lu, P. Jiang, X. Bao, *Adv. Mater.* **2022**, 34, 2204355.